한국공작기계학회 '98년도 춘계학술대회 논문집 pp. 40~52

Understanding the Material Removal Mechanisms of Abrasive Water Jet Drilling Process by Acoustic Emission Technique

Kwak Hyo-Sung* and Radovan Kovacevic**
*LG-EDS Systems Inc. CALS/CIM Division
**Department of Mechanical Engineering
Southern Methodist University
Dallas, TX
U.S.A.

ABSTRACT

Among the non-traditional machining methods, Abrasive waterjet machining process shows big promise in drilling difficult-to-machine materials due to its numerous advantages such as absence of heat affect zone and thermal distortion. Acoustic emission signal technique is used to understand about material removal mechanisms during abrasive waterjet drilling process. More information about the drilling process is derived through frequency decomposition of auto regressive moving average modeling representing acoustic emission signals.

1. INTRODUCTION

Abrasive waterjet (AWJ) cutting technique can be considered as one of the most recent non-traditional manufacturing processes to be introduced. In this technique, the material removal is primarily through the erosive action of abrasive particles which are accelerated by a thin stream of high velocity waterjet and are directed through a nozzle. AWJ cutting was first introduced as a commercial system in 1983 for cutting glass. Nowadays, this process is being used widely for machining difficult-to-machine materials like ceramics, ceramic composites, metal matrix composites, fiber-reinforced resin composites, titanium and its alloys, etc., where conventional machining processes are often not technically or economically feasible. High speed and multidirectional cutting capability, high cutting efficiency to cut complicated shapes of even nonflat surfaces very effectively at close tolerances, easy accomplishment of changeover of cutting patterns under computer control, etc., are a few of the advantages offered by this process which makes it ideal for a flexible manufacturing environment. Originally, the abrasive waterjet machining technology was applied for linear cutting and shape cutting of these materials. However, recently this technology is used for such machining applications as milling, turning, screw thread and drilling.

There have been few studies on understanding of mechanisms AWJ drilling process. Hashish et al. [1] used sound measurements for the ceramic thermal barrier coating material drilling process. It was observed that changes in the noise level while drilling is indicative of fracturing. However, no distinction could easily be made while drilling through the layers of the material if no fracturing occurs. The first analytical investigation into the mechanisms of AWJ drilling process was performed by Raju and Ramulu[2]. They have reported a semi-transient numerical model for prediction of the depth of AWJ drilling. The model was developed to obtain an approximate mean velocity distribution in the cavity based on principle of energy conservation. However, the experimental results were not closely machining the model predictions especially at extremely low or high drilling depths.

Recently acoustic emission(AE) signals have been widely used in monitoring manufacturing processes [3-5]. In field of abrasive water jet cutting technology, Mohan et al. [6] have applied AE technique for monitoring of depth of cut in grey cast iron. They found that the power spectrum density of the auto regressive moving average model, representing the time domain AE signals gave an indication of the depth of penetration. Momber et al. [7] used acoustic emission sensing technique for on-line monitoring of abrasive waterjet cutting of brittle materials. AE signals measured and analyzed for different process parameters, such as pump pressure, traverse rates, and abrasive flow rate. The results demonstrated that acoustic emission signals were capable of revealing the different material removal mechanisms in brittle materials. Mohan et al. [8] proved that AE signals generated in a AWJ cutting process were related to energy absorption in the workpiece.

Stochastic modeling has been applied in AWJ cutting process[9-11]. Kovacevic et al. [9] have investigated surface texture using stochastic modeling. It can be seen that stochastic model characterization has provided information about the nature of abrasive waterjet cutting process. A novel method of auto regressive moving average(ARMA) model is utilized for surface profile and dynamic force characterization[10]. More information about surface profiles is derived through wavelength decomposition of the ARMA models. The peak of the power spectrum density(PSD) of the ARMA models representing the dynamic workpiece normal force signal can be considered as a potential parameter for on-line monitoring of the surface finish.

2. STOCHASTIC MODELING PRINCIPLES

Auto regressive moving average modeling has been considered as an effective tool for signal processing. However, there is no suitable approach for selecting an optimum interval for ARMA characterization. Furthermore, the accuracy requirement varies from case to case. Hence, more data is expected to be processed for more accurate results. The computational burden prevents one from selecting extensive data. In fact, since the parameter estimation of the ARMA model is non-linear and since the computational burden of the conventional methods (for example, the non-linear least squares (NLS) method [12] and maximum likelihood (ML) method [13]) are proportional to the sample sizes, the identification of large samples will be time consuming. Therefore, an alternative algorithm for identifying ARMA models has been proposed [10] based on the concept of model distance.

The aim of this approach is to decrease the computational burden to accuracy ratio, with reliable evaluation of the final modeling accuracy. The procedure for the proposed approach consists of two steps.

(1) Auto regressive (AR) modeling - Identifying an AR model from the samples

(2) ARMA approximation - Identifying the ARMA model based on this AR model.

It has been shown that by this method [19] that the modeling accuracy to computational burden ratio increases with sample size, whereas this ratio nearly constant for conventional methods. Also, its computational burden is nearly independent of sample size. This makes it possible for one to adequately utilize extra-large samples to improve the modeling accuracy without virtual increase in computational burden. ARMA models will be identified here using this approach. Model distance method has been proven for its capability to handle large data sets with improved modeling accuracy [9, 10]. This approach is used for analysis of AE data.

2.1. MODEL DISTANCE FOR AR AND ARMA MODELING

For obtaining the dynamic characteristics of the AE data, it needs to be modeled using stochastic modeling technique. It can be obtained the difference equation model directly from the data by fitting using suitable ARMA(p,q) model. The ARMA (p,q) model can be represented by the equation,

$$Y_t - \phi_1 Y_{t-1} - \phi_2 Y_{t-2} - \ldots\ldots - \phi_p Y_{t-p} = a_t - \Theta_1 a_{t-1} - \Theta_2 a_{t-2} - \ldots\ldots - \Theta_q a_{t-q} \tag{1}$$

where, Y_t is the amplitude of the signal at time t, a_t is the noise, $a_t \sim NID\ (0, \sigma^2_a)$, NID is normally independently distributed, and σ^2_a ia variance. It may be noted that Y_t is independent of Y_{t-1}, Y_{t-2},..., Y_{t-p} and a_t , a_{t-1},...,a_{t-p}.

The power spectrum density function of the ARMA(p,q) model, which is the transform of auto co-variance function is given [12] by the equation,

$$p(f) = 2\sigma_a^2 \frac{|1 - \theta_1 e^{-i2\pi f} - \theta_2 e^{-i4\pi f} - \ldots\ldots - \theta_q e^{-i2\pi qf}|^2}{\gamma_0 |1 - \phi_1 e^{-i2\pi f} \phi_2 e^{-i4\pi f} - \ldots\ldots - \phi_p e^{-i2\pi pf}|^2} \tag{2}$$

where $i^2 = -1$, and $0 \le f \le 1/2$.

The power spectrum density of the best fit ARMA model is obtained for further analysis. The dynamic characteristics of the system can be interpreted from these plots.

The frequency decomposition of the roots of the ARMA (p,q) model can be derived [14] from each complex root, say, $\kappa_{1,2}$ is complex. It has a damped natural frequency given by,

$$f_d = \frac{1}{2\pi\Delta} \arccos\left[\frac{x}{\sqrt{x^2 + y^2}}\right] \tag{3}$$

where, Δ is the sampling length in seconds.

To distinguish between different real roots causing different concentration of frequencies around zero, a pseudo frequency called break frequency, corresponding to half power point is obtained for each real root. The break frequency of a real root, say $\kappa_3 = z$, is given by,

$$f_b = \frac{-\ln|z|}{2\pi\Delta} \tag{4}$$

It may be noted that variance decomposition (d_i) of each root gives the relative power of the root.

3. EXPERIMENTAL SETUP AND PROCEDURES

Experimental work was conducting for monitoring abrasive waterjet drilling process. A schematic of the abrasive waterjet drilling system with acoustic emission measurement is shown in Fig.1. It consists of a abrasive waterjet drilling system and acoustic emission monitor system. The generated acoustic emission signals were detected and processed by Model AET 5500 Acoustic Emission Monitoring System which consists basically of AET 5500 mainframe, graphics terminal and the accessories (sensors, pre-amplifier). When an acoustic emission caused by an induced stress occurs in a test specimen, the sensors (resonant frequency 2 MHz) convert this acoustic wave into a voltage signal which is amplified by the pre-amplifier and sent to the mainframe (16-bit microprocessor) for post processing. For detecting the acoustic emission signals from the abrasive waterjet drilling process, a sensor was fixed on the side wall of the workpieces with a water resistant epoxy-gum. Three types of non-homogeneous refractory ceramics namely magnesia chromite, sintered magnesia, and bauxite ceramics of 51 mm thickness were used. Their material properties and composition are shown in Table 1.

Acoustic emission signals were acquired at a sampling frequency of 1 MHz (at a pre-amplifier gain of 100.0 and amplifier gain of 5.0) with progressive drilling time. The sampling frequency for acoustic emission signals was chosen such that the complete energy of the signals was covered in the respective frequency range. Acoustic emission signals were monitored during the drilling process, where the target material is subjected to erosion by abrasive water mixture. The time domain acoustic emission signal was acquired in several data sets over the entire drilling process. Each data set consists of 1024 data points representing the acoustic emission signal generated at a particular instant of time. Stochastic modeling of these time domain signals is performed through ARMA modeling technique. All these experiments were performed several times for the same set of process parameters and workpiece material to verify the repeatability of the results. The process parameters adopted are given in Table 2. The results of this experimental study are given below followed by a brief discussion.

4. RESULTS AND DISCUSSION

Even though Fast Fourier Transform (FFT) and PSD represent the power of the AE signal, FFT is derived from the time domain data, whereas PSD is derived from the ARMA model representing the time domain data. Area under the PSD curve can be considered as a better representative of the power of the AE signals as it is devoid of white noise. Fig. 2 (a), (b) and (c) show the plot of PSD area against drilling time for magnesia chromite, sintered magnesia and bauxite respectively. It can be noted that magnesia chromite and sintered magnesia have two separately identified linear regions. Whereas bauxite has three linear region. The critical depths are marked in the respective figures. The critical depth is higher for material with lower compression strength. In these materials, until the critical depth is reached the damping effect of the rebounded jet is not significant. However, after the critical depth, the trend becomes more shallow due to the increased damping effect of the rebounded jet. The three regions of bauxite material are discussed below in detail.

In order to better understand the material removal mechanism in the three materials, time domain signals representing each region were plotted separately. Fig. 3 (a) and (b) represent the time domain signal corresponding to points (a) and (c) of Fig. 2 (a) for magnesia chromite material. It can be noted that these time domain AE signals are of continuous type representing a material removal mechanism due to intergranular erosion. Lower Young's

modulus and lower cold compressive strength of magnesia chromite is indicative of ductile behavior. In such materials, presence of hard inclusions and much softer matrix contribute to a material removal mechanism of intergranular erosion. Results of visualization studies given later also support this observation.

Figure 4 (a) and (b) represent the time domain signal corresponding to points (a) and (c) of Fig. 2 (b) for sintered magnesia material. Similar to magnesia chromite, these time domain signals are also of continuous type but much denser. High Young's modulus and relatively low cold compressive strength of this material are indicative of a highly brittle nature. From the composition it is evident that this material is primarily a homogeneous material. In this background, the presence of a highly dense continuous mode AE signal is indicative of a material failure due to continuous generation of micro-crack network. The AE signal during AWJ drilling of glass is shown in Fig. 5. It is known that material failure in glass during impingement with AWJ is primarily due to continuous generation of micro-crack network. The fact that both the AE signals represented by Fig. 4 (b) and Fig. 5 are of similar type is also an indication of above material failure mode.

Figures 6 (a-e) are the time domain AE signal of bauxite material representing points a to f in Fig. 2 (c). Figure 6 (a) representing region I of Fig. 2 (c) is predominantly of a burst emission type. Figure 6 (b) and (e) representing region II of Fig. 2 (c) for bauxite material are predominantly continuous type signals. Whereas Figs. 6 (c) and (d) representing region III of Fig. 2 (c) are predominantly burst type signal. This indicates that due to high compressive strength material removal occurring in bauxite material is primarily transgranular fracture type. Region II of Fig. 2 (c) consists of material removal from the soft matrix and region III represents material removal through transgranular fracture of hard inclusion.

Frequency decomposition of the ARMA model representing the AE signals is performed to understand more about physics of the material removal process in AWJ drilling. Table 3, 4 and 5 show the results of the frequency decomposition of magnesia chromite, sintered magnesia and bauxite respectively. These tables indicate the primary and secondary roots of the ARMA model representing each data set.

From Table 3, it can be noted that all the primary roots have complex roots which denote an exponentially decaying dynamic model. It can also be seen that the power of the primary root reduces and that of the secondary root increases gradually until the critical depth (point b of Fig. 2(a)) is reached. The frequency range of the primary root is 120 KHz to 160 KHz, whereas most of the secondary frequencies are observed in the range of 70 KHz to 180 KHz. The impinging jet can be considered as responsible for the primary root and the rebounded jet can be considered as responsible for the secondary root. Above trend indicates that with progressive depth of drilling the effect of the impinging jet reduces and that of the rebounded jet increases. Beyond the critical depth, the presence of rebounded jet in the narrow hole creates turbulence and hence affects the penetration process. The damping effect of the rebounded jet is also indicated by the negative power of the secondary root at larger depths and the presence of negative real roots.

In the case of sintered magnesia (Table 4) all the primary roots and almost all the secondary roots are complex roots. The frequency and power of the primary root reduces and that of the secondary root increases gradually until the critical depth (point b of Fig. 2(b)) is reached. Beyond the critical depth the power of the secondary frequency increases further that there is a switch between the primary and the secondary root. The primary frequency after the critical depth can be observed in the range of 200 KHz to 330 KHz, whereas the secondary frequency is in the range of 140 KHz and 180 KHz. This frequency range is different from that observed in the case of magnesia chromite. Presence of negative power of the secondary frequency and the frequency shift at higher depths indicate the increased

damping effect of the rebounded jet.

For bauxite (Table 5) the primary frequency is observed in the range of 120 KHz to 200 KHz for all depths whereas the secondary frequency is in the range of 60 to 90 KHz until a depth of 40 mm. Beyond 40 mm depth the secondary frequency increases gradually. This increase in secondary frequency indicates increased damping effect at larger depths. This trend in the bauxite material also supports the view that primary frequency is caused by the impinging jet and secondary frequency is caused by the rebounded jet. However, the presence of a failure mode due to transgranular fracture produces a combination of weak and strong signals from the soft matrix and hard inclusions respectively. This is responsible for lack of clear trend in the power of the roots with drilling depth.

5. CONCLUSIONS

Acoustic emission sensing technique provides critical information about the material removal mechanisms in AWJ drilling process. Material removal in ceramic materials exhibiting ductile behavior is primarily due to intergranular erosion indicated by sparse continuous emission AE mode. The material removal in highly brittle materials in AWJ drilling is primarily due to continuous propagation of micro-cracking network as indicated by dense continuous emission AE mode. Material failure in high compressive strength materials is caused by transgranular fracture indicated by a predominantly burst emission signal.

Stochastic modeling of acoustic emission signals provides insight into the physics of the abrasive waterjet drilling process. For each material, the impinging jet is dominant until a critical depth beyond which the damping effect or the rebounded jet becomes predominant. Frequency decomposition of the ARMA model indicates that primary frequency of the AE signal is caused by the impinging jet and secondary frequency is caused by the rebounded jet.

REFERENCES

1. Hashish. M., and Whalen. J., "Precision Drilling of Ceramic-Coated Components with Abrasive-Waterjets". *ASME. J. of Engr. for Gas Turbines and Power.* Vol. 115. pp.148-154. 1993.

2. Raju. S. P., and Ramulu, M. "A Transient Model for Material Removal in the Abrasive Waterjet Machining Process." *Proc. of 7th American Water Jet Conference.* Seattle, Washington. pp. 141-155. Aug. 1993.

3. Liu. J. J., and Dornfeld. D. A., " Monitoring of Micromachining Process using Acoustic Emission." *Transaction of NAMRI/SME.* Vol.XX. pp.189-195. 1992.

4. Blum. T., and Inasaki. I., "A study on Acoustic Emission from the Orthogonal Cutting Process." *ASME, J. of Engineering for Ind.* Vol.112. pp. 203-211. Aug. 1990.

5. Emel. E., and Kannatey-Asibu, E., "Acoustic Emission Monitoring of the Cutting Process-Negating the Influence of Varying Conditions." *ASME. J. of Engineering Materials and Technology.* Vol. 113. pp. 456-464. Oct. 1991.

6. Mohan. R., Momber. A., and Kovacevic. R., "On-Line Monitoring of Depth of AWJ Penetration Using Acoustic Emission Technique." *Waterjet Cutting Technology,* Mechanical Engineering Publication. Suffolk. pp. 649-664. 1995.

7. Momber. A., Mohan. R., and Kovacevic. R., "Acoustic Emission Measurements on Brittle Materials during Abrasive Waterjet Cutting". *First Int'l Machining and Grinding Conference. MR95-184* pp.439-458, Dearborn, MI. Sept. 1995.

8. Mohan. R., Momber. A., and Kovacevic. R., "Detection of Energy Absorption During Abrasive Waterjet Machining Using Acoustic Emission Technique." *ASME Manufacturing Science and Engineering MED.* Vol. 2-1, pp.69-85. 1995.

9. Kovacevic. R., Mohan. R., and Zhang, Y. M. "Stochastic Modeling of Surface Texture Generated by High-Energy Jets." *Proc. of the Institute of Mechanical Engineers, Part B, Journal of Mechanical Engineering Science,* Vol. 207. pp. 129-140. 1993.

10. Kovacevic. R., and Zhang, Y. M., "Identification of Surface Characteristics from Large Samples." *Proc. of the Institute of Mechanical Engineers, Part C, Journal of Mechanical Engineering Science,* Vol. 206. pp. 275-284. 1992.

11. Kovacevic. R., Mohan. R. and Zhang. Y. M., " Cutting Force Dynamics as a Tool for Surface Profile Monitoring in AWJ

12. Pandit. S. M. and Wu.M., "*Time Series and System Analysis with Applications.*" John Wiley & Sons, New York. 1983.

13. Box. G. E. P. and Jenkins. G. M., "*Time Series Analysis, Forecasting and Control.*" Holden Day, California. 1976.

14. Pandit, S. M., and Shunmugam, M. S., "Signature of Machine Tool Errors on Surface Texture by DDS," *ASME, J. of Engineering for Ind.* Vol. 114. pp. 370-374. 1992.

Table 1. Material Properties and Composition

Material	Density (g/cm^3)	Porosity (%)	Cold Compressive Strength (MPa)	Cold Bend. Tensile Strength (MPa)	Young's Modulus (MPa)	Composition (%)
Magnesia Chromite	3.26	15.20	30.00	3.50	13,000.00	Al_2O_3-8, Fe_2O_3-14, SiO_2-0.5, MgO-60, CaO-1.3, Cr_2O_3-18
Sintered Magnesia	3.00	15.20	40.00	14.00	85,000.00	Al_2O_3-0.1, Fe_2O_3-0.2, SiO_2-0.5, MgO-97, CaO-2.1
Bauxite	2.89	15.00	126.00	19.00	59,000.00	Al_2O_3-81, Fe_2O_3-1.7, SiO_2-12, CaO+MgO-0.4, TiO_2-3.2, K_2O+Na_2O-18

Table 2. Process Parameters

Parameter	Value
Abrasive Material	Garnet
Abrasive Mesh Size	80
Abrasive Particle Shape	Angular (random)
AWJ Orifice Material	Sapphire
AWJ Orifice Diameter	0.46 mm
Mixing Nozzle Diameter	1.27 mm
Mixing Nozzle Length	88.9 mm
Method of Feed	Suction
Condition of Abrasive	Dry
Angle of Jet	90°
Material Thickness	51 mm
Pump Pressure	206 Mpa
Abrasive Flow Rate	5.75 g/s
Stand-off Distance	5 mm
Materials	Magnesia Chromite, Sintered Magnesia, Bauxite

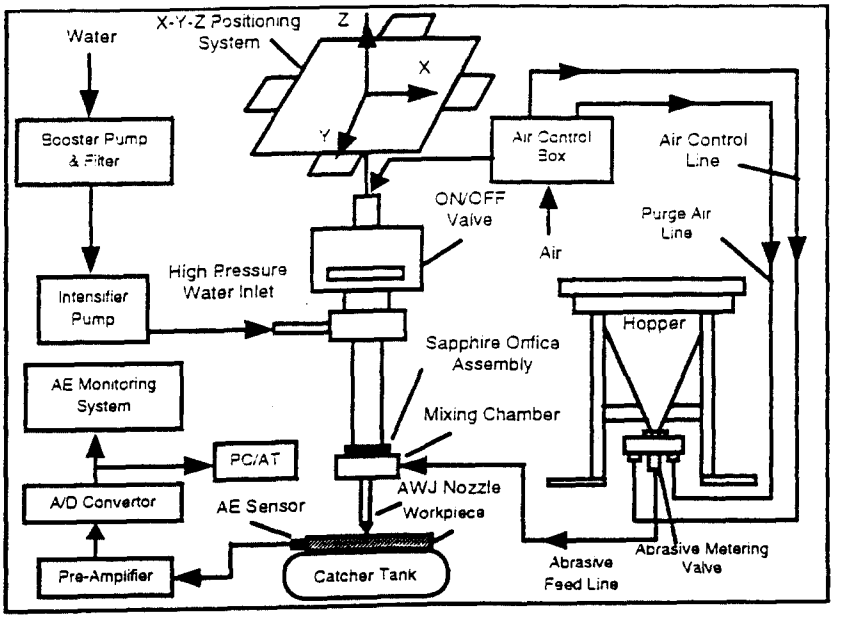

Figure 1. Experimental Setup

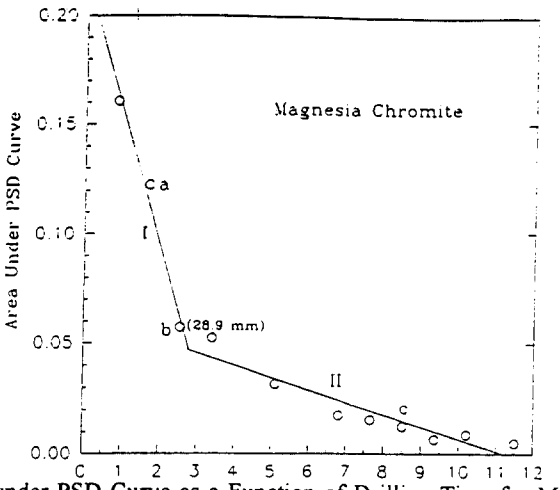

Figure 2 (a). Area under PSD Curve as a Function of Drilling Time for Magnesia Chromite

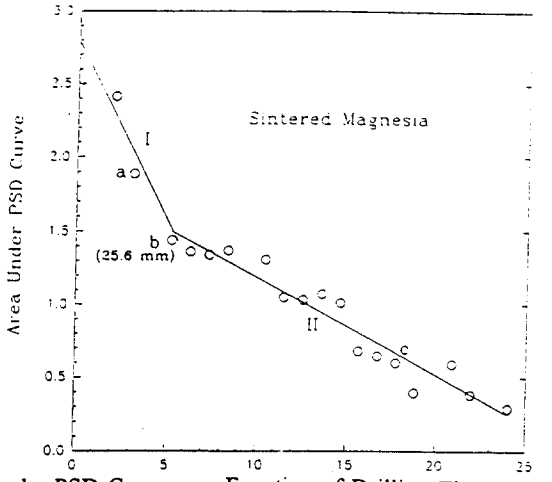

Figure 2 (b). Area under PSD Curve as a Function of Drilling Time for Sintered Magnesia

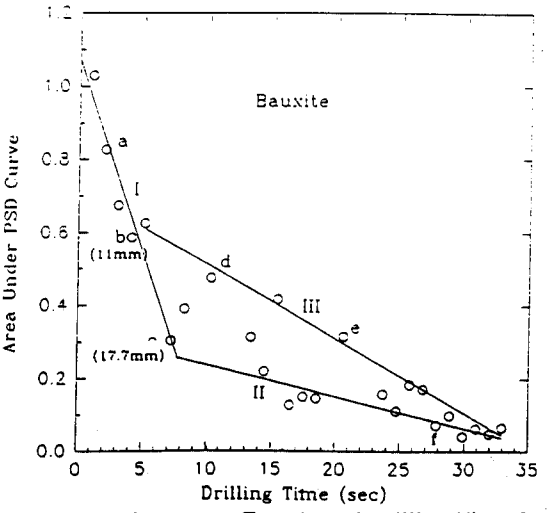

Figure 2 (c). Area under PSD Curve as a Function of Drilling Time for Bauxite

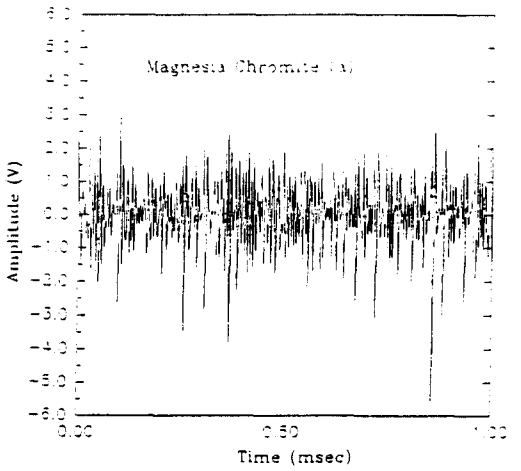

Figure 3 (a). Time Domain Signal for Stage (a)

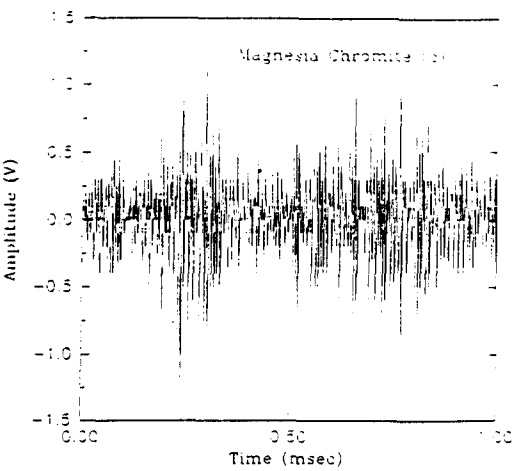

Figure 3 (b). Time Domain Signal for Stage (c)

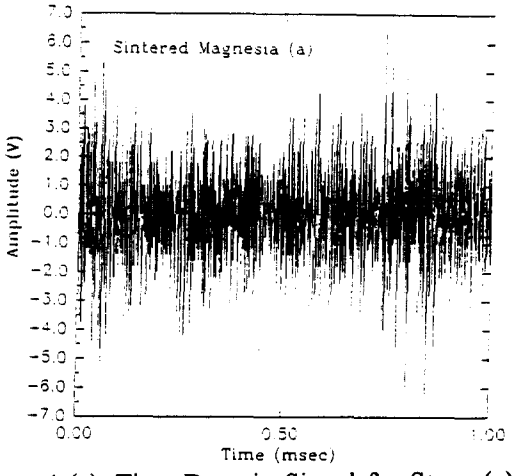

Figure 4 (a). Time Domain Signal for Stage (a)

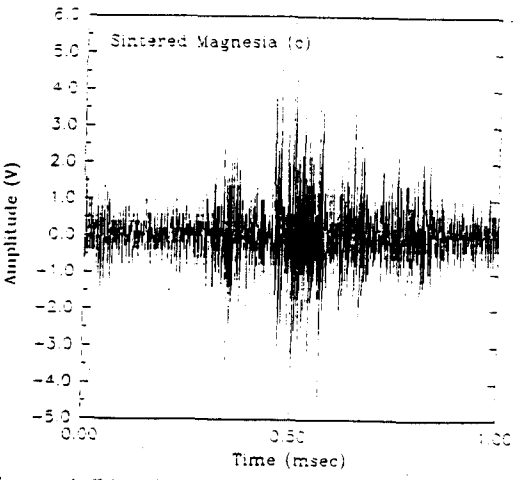

Figure 4 (b). Time Domain Signal for Stage (c)

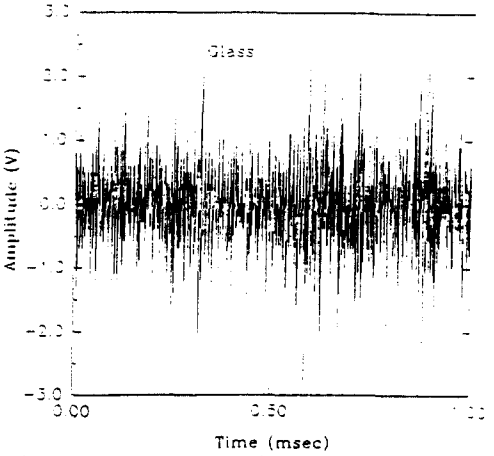

Figure 5. Time Domain Signal for Glass

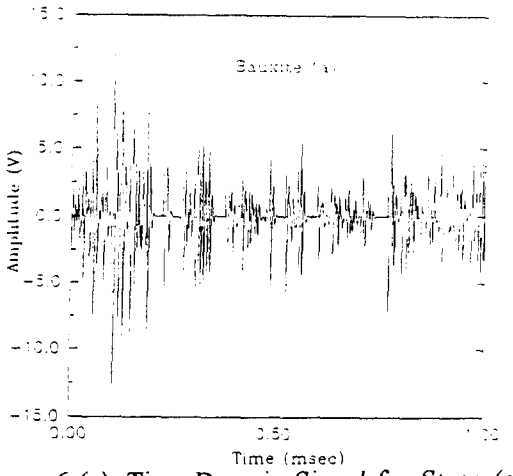

Figure 6 (a). Time Domain Signal for Stage (a)

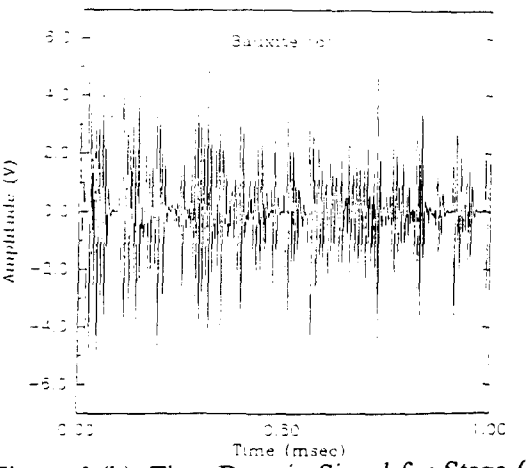

Figure 6 (b). Time Domain Signal for Stage (c)

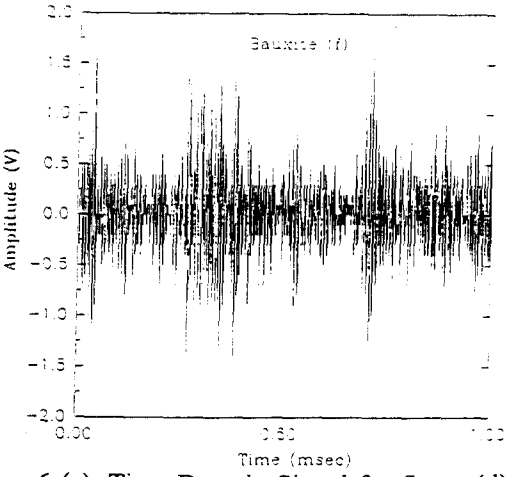

Figure 6 (c). Time Domain Signal for Stage (d)

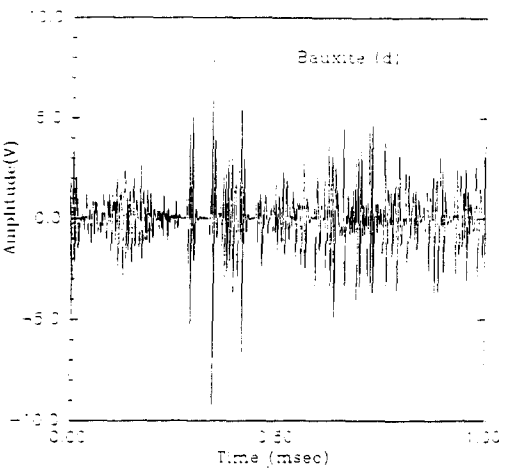

Figure 6 (d). Time Domain Signal for Stage (e)

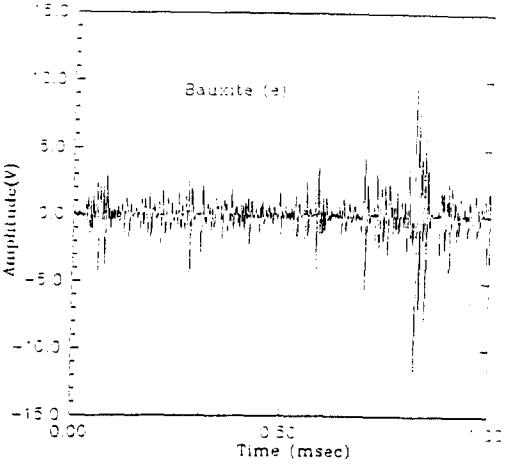

Figure 6 (e). Time Domain Signal for Stage (f)

Table 3. Frequency Decomposition- Magnesia Chromite

Time (sec)	Depth (mm)	Root (1)Primary (2) Secondary	Discrete		Frequency (MHz)	Power (%)
			Real	Imaginary		
0.85	9.57	1	0.5204	±0.6172	0.1385	80.10
		2	0.7901	±0.3851	0.0722	19.90
1.70	17.37	1	0.5026	±0.6693	0.1475	78.62
		2	0.8119	±0.3846	0.0704	21.38
2.55	23.73	1	0.4938	±0.6766	0.1497	55.14
		2	0.8142	±0.4418	0.0791	44.86
3.40	28.92	1	0.7539	±0.5087	0.0945	51.50
		2	0.4556	±0.7412	0.1623	48.50
5.10	36.59	1	0.5276	±0.6447	0.1408	99.12
		2	-0.5842	±0.3528	0.4135	0.88
6.80	41.70	1	0.4950	±0.7663	0.1587	65.4
		2	0.8020	±0.4740	0.1132	34.6
7.65	43.57	1	0.5619	±0.7144	0.1439	98.72
		2	-0.3328	±0.0000	0.1751	1.28
8.50	45.10	1	0.534	±0.7354	0.1501	94.08
		2	-0.0610	±0.0000	0.4451	5.92
9.35	46.34	1	0.6109	±0.5783	0.1206	126.78
		2	0.2760	±0.6249	0.1838	-26.78
10.20	47.36	1	0.4986	±0.7606	0.1577	94.76
		2	-0.2204	±0.0000	0.2407	5.24
11.50	48.20	1	0.5544	±0.5856	0.1294	155.88
		2	0.1761	±0.3849	0.1817	-55.88

Table 4. Frequency Decomposition-Sintered Magnesia

Time (sec)	Depth (mm)	Root (1)Primary (2)Secondary	Discrete		Frequency (MHz)	Power (%)
			Real	Imaginary		
2.08	12.68	1	0.1964	±0.5471	0.1951	96.36
		2	-0.8960	±0.0000	0.0175	3.63
3.13	17.76	1	0.4592	±0.6358	0.1505	63.82
		2	0.1917	±0.0000	0.2629	36.18
5.21	25.95	1	0.5308	±0.6781	0.1443	50.14
		2	-0.4020	±0.5925	0.3449	40.50
6.26	29.23	1	-0.3757	±0.5416	0.3465	56.96
		2	0.4978	±0.6374	0.1445	33.20
7.30	32.07	1	-0.1251	±0.6525	0.2801	52.20
		2	0.5282	±0.6829	0.1452	41.32
8.35	34.52	1	-0.2247	±0.6645	0.3162	71.76
		2	0.5082	±0.7706	0.1572	28.24
10.43	38.48	1	-0.0032	±0.6585	0.2508	79.14
		2	0.5018	±0.7746	0.1585	20.86
11.48	40.07	1	-0.0565	±0.6017	0.2649	68.74
		2	0.4792	±0.7386	0.1584	31.26
12.52	41.44	1	-0.3335	±0.5255	0.3400	59.36
		2	0.4521	±0.6564	0.1540	30.58
13.57	42.62	1	-0.1043	±0.7330	0.2725	79.52
		2	0.4940	±0.7341	0.1557	20.48
14.61	43.64	1	-0.0358	±0.6530	0.2587	82.46
		2	0.4925	±0.7129	0.1538	17.54
15.65	44.53	1	0.0194	±0.6826	0.2455	80.28
		2	0.4861	±0.7400	0.1575	19.72
16.70	45.30	1	-0.1878	±0.6277	0.2963	76.32
		2	0.5120	±0.7282	0.1525	23.68
17.74	45.96	1	-0.1477	±0.6079	0.2879	74.68
		2	0.4924	±0.6660	0.1487	25.32
18.78	46.53	1	0.0788	±0.5272	0.2264	138.08
		2	-0.3230	±0.0000	0.1799	-38.08
19.83	47.03	1	0.1571	±0.4975	0.2013	115.16
		2	-0.5404	±0.0000	0.0979	-15.16
20.87	47.45	1	-0.3157	±0.6424	0.3227	66.16
		2	0.4388	±0.7477	0.1655	33.84
21.91	47.82	1	-0.0977	±0.6747	0.2729	72.52
		2	0.4703	±0.7429	0.1602	27.48
24.00	48.42	1	-0.2974	±0.5817	0.3252	73.00
		2	0.4816	±0.7138	0.1555	13.00

Table 5. Frequency Decomposition- Bauxite

Time (sec)	Depth (mm)	Root (1)Primary (2)Secondary	Discrete		Frequency (MHz)	Power (%)
			Real	Imaginary		
1.03	2.99	1	0.4644	±0.5844	0.1431	65.56
		2	0.7676	±0.4333	0.0818	34.44
2.06	5.81	1	0.4775	±0.6162	0.1451	78.2
		2	0.7705	±0.4049	0.0770	21.8
3.09	8.47	1	0.4606	±0.5756	0.1426	70.68
		2	0.7719	±0.4150	0.0782	29.32
4.12	10.99	1	0.4991	±0.5986	0.1394	102.34
		2	0.7374	±0.3698	0.0739	-2.34
5.15	13.37	1	0.4826	±0.6277	0.1457	88.68
		2	0.7719	±0.3797	0.0728	11.32
7.21	17.74	1	0.5565	±0.6708	0.1398	100.0
8.24	19.75	1	0.3865	±0.6041	0.1594	51.18
		2	0.7576	±0.4815	0.0901	48.82
10.3	23.44	1	0.5055	±0.6944	0.1498	100.0
13.39	28.25	1	0.4575	±0.5339	0.1372	64.04
		2	0.7743	±0.4059	0.0768	35.94
14.42	29.68	1	0.4445	±0.5859	0.1467	70.40
		2	0.7930	±0.4672	0.0847	40.82
15.45	31.03	1	0.4535	±0.5736	0.1435	70.50
		2	0.7697	±0.4141	0.0786	29.50
16.48	32.30	1	0.5130	±0.6684	0.1458	100.0
17.51	33.51	1	0.4821	±0.6156	0.1442	84.26
		2	0.7829	±0.3420	0.0656	15.74
18.54	34.65	1	0.5050	±0.5841	0.1365	101.96
		2	0.7755	±0.3128	0.0610	-1.96
20.6	36.74	1	0.5616	±0.5752	0.1269	111.34
		2	0.7584	±0.3097	0.0617	-11.34
23.69	39.47	1	0.3395	±0.6653	0.1749	65.0
		2	0.7815	±0.4279	0.0797	35.0
24.72	40.28	1	0.4386	±0.6909	0.1608	99.86
		2	-0.6597	±0.0000	0.0662	0.28
25.75	41.05	1	0.3638	±0.6306	0.1724	59.22
		2	0.6032	±0.5839	0.1224	40.78
26.78	41.77	1	0.2311	±0.6899	0.1986	61.78
		2	0.6434	±0.5744	0.1160	38.22
27.81	42.46	1	0.6418	±0.6285	0.1233	76.54
		2	0.0712	±0.7185	0.2043	23.46
28.84	43.11	1	0.6641	±0.6171	0.1192	75.28
		2	0.1280	±0.5414	0.2131	20.78
29.87	43.72	1	0.6285	±0.6025	0.1216	53.64
		2	0.2835	±0.6610	0.1855	46.36
30.90	44.29	1	0.5870	±0.6541	0.1336	103.36
		2	0.0366	±0.6407	0.2409	-3.36
31.93	44.84	1	0.6095	±0.6536	0.1306	84.92
		2	0.1285	±0.7152	0.2217	15.08
32.96	45.35	1	0.5763	±0.6561	0.1353	84.0
		2	0.0817	±0.6888	0.2312	16.0